Numerical Simulation of Blood Flow through Different Stents in Stenosed and Non-Stenosed Vessels.

Andrea Boghi[a], Fabio Gori[b,*]

[a] Applied Mathematics and Computing Group, School of Engineering, Cranfield University, Cranfield, Bedfordshire MK43 0AL, United Kingdom, a.boghi@cranfield.ac.uk.

[b] University of Rome “Tor Vergata”, Via del Politecnico 1, 00133 Rome, Italy.

[*] Corresponding Author, fammannati@yahoo.com.

Short title: Blood Flow in stenosed and non-stenosed stent.

Abstract

The fluid dynamics in two different stent configurations, peak-to-valley (S1) and peak-to-peak (S2), within a fully expanded situation and a 30% restenosis, is investigated. Numerical simulations are carried out in order to evaluate the conditions promoting atherosclerotic events when a self-expanding bare metal stents (SE-BMS) is applied. The conclusions are that the two configurations, S1 and S2, have a similar fluid dynamic behavior, as far as the WSS is concerned, but OSI and RRT maps suggest that the peak-to-peak configuration, S2, has a better behavior than the peak-to-valley one, S1.

Key words: stent, stenosis, wall shear stress, OSI, RRT

1. Introduction

Cardiovascular diseases, such as coronary artery stenosis, represent the main cause of death in western countries. Among these atherosclerosis, a condition of chronic inflammatory response in the endothelium of large and medium arteries leading to wall thickening and eventually vessel obstruction, is one of the most widespread. Despite its pathogenesis is not fully understood yet, various anatomical, physiological and behavioral risk factors, such as diabetes, advanced age and obesity [1], have been identified.

A large number of studies in the past two decades have demonstrated the existence of a correlation between flow field conditions and commonly developing atherosclerosis [2-3]. The regions subject to low and oscillatory wall shear stress, i.e. those presenting flow stagnation, represent the locations where these diseases preferentially occur [2-6]. Indeed, a locally increased residence time could lead to an enhanced uptake of macrophages and macromolecules, such as LDL (low density lipoprotein), by intimal smooth muscle cells [7]. Inflammatory cells and LDL infiltration in the sub endothelial space lead to a stable narrowing of the vessel lumen (stenosis). Even when the atheroma does not ulcerate, thrombosis and ischemia can occur. This could cause the blood flow to be insufficient to meet the metabolic demand, especially during exercise.

The introduction of intravascular stents, to restore the lumen of the stenotic vessels, has brought great improvements, in term of quality of life in patients suffering from this disease. However, some problems, related to the use of stent, remain. The stent is recognized as a foreign body and is covered with endothelial cells (EC), whose uncontrolled proliferation can lead to restenosis of the vessel, making, in some cases, a new angioplasty operation necessary.

This problem can be tackled with drug eluting stents (DES) which show good clinical responses with a low restenosis rate [8], but seems to have the same clinical outcome of bare metal stents (BMS) and self-expanding bare metal stents (SE-BMS) at 12 months follow-up, as far as

restenosis concerns [9]. These devices are unable to heal intima damaged by stent implantation procedure, which can be limited by slightly oversized SE-BMS as shown in [10]. Nonetheless, the residual stenosis after the implant, even if not significant in terms of reduction of the flow rate, may represent a critical location for the hemodynamics. Moreover, there is good evidence that arterial injuries, caused by both balloons and stents, lead to an inflammatory response and activates a proliferative repair process, which can lead to luminal narrowing and in-stent restenosis [11-12].

The carotid artery is one of the most common locations of cranio-cervical atheromatous diseases, accounting for 20- 30% of strokes. Often, these conditions are result of detachment of thrombo-embolic material from the atheromatous plaque [13]. This problem has been investigated numerically, in a realistic geometry in [14] where the non-Newtonian features of blood have been take into account as well, while the non-Newtonian behaviour of the fluid in turbulent flow has been investigated in [15-17] and the characteristics of mass diffusion in [18-19]. Although carotid angioplasty and stenting have recently emerged as valid therapeutic alternatives to carotid endarterectomy, risks associated with embolic complications are still high, ranging from 4% to 33%, and slowing down the introduction of the technique in the carotid circulation, as compared with the coronary and peripheral arteries [20-21].

Both two-dimensional (2D) and three dimensional (3D) computational fluid dynamics (CFD) simulations have been performed in arteries restored by stents. Two-dimensional CFD studies employed simple stent geometries to investigate the influence on the blood flow of the mesh size [22], the shape of the struts section [23] and the design near the curvatures [24], trying to understand how these geometric features can be tuned to change the hemodynamics. LaDisa et al. [25-26] have performed several 3D CFD simulation on different geometries and stent design, analyzing how 3D geometric parameters, i.e. intra-strut angles, width and connector styles, can affect the distribution of plaques. Gori at al. [27-29] have carried out 3D CFD simulations on commercial coronary stents, employing different parameters to identify critical points for the

hemodynamics and suggesting guidelines for the design of optimal implants to avoid restenosis. The fluid has been considered Newtonian in [27-28] while the influence of non-Newtonian blood features has been investigated in [29].

The aim of the present work is to investigate the blood flow in two carotid self-expanding bare metal stents (SE-BMS), under physiologic conditions, and in a non-completely restored vessel lumen by 3D CFD simulations. The last situation is likely to occur in SE-BMS graft.

2. Geometry and mesh

The simulations are carried out on two different stents, reported in Fig. 1, in order to assess the influence of the different configurations on the fluid-dynamics. The stent of Fig. 1a , named S1, has the strut tips arranged in the same direction, according to a configuration called peak-to-valley, while that of Fig. 1b, named S2, has the struts arranged in the opposite way, and is called peak-to-peak. Both stents are applied to the carotid artery (8 mm in diameter), modeled as a cylindrical tube, in one case with constant section, and in the other one with a slight reduction of the radius in the middle section. Geometrical parameters of the stents are chosen from [30], to match an artery with the diameter of 8 mm, stent radial thickness is 0.122 mm while the two lengths are respectively 24.8 mm and 22.9 mm. The simulations are not been carried out in the entire cylindrical domain because of the radial symmetry, but only in one-sixth of the geometry, as done in [27], allowing significant saving in computational time. The choking in the middle section has a radius of 6.8 mm, corresponding to an area reduction of 30 %.

$$P(\%) = 100 \cdot \left(1 - \left(\frac{R_2}{R_1} \right)^2 \right) \qquad (1)$$

The stenosis profile, represented in Fig. 2, is reproduced by a piecewise cubic spline interpolation of ten control points. The mesh used, generated with the commercial code STAR-CCM+ 8.02.011, refined with SolidWorks 2010 and reported in Fig. 3, is made of tetrahedral

elements in the core of the vessel, while near the wall a prismatic layer is employed. The grid is not uniform but coarser near the centerline and finer towards the wall and near the struts.

3. Governing equations

The 3D incompressible Navier-Stokes equations govern the mass and momentum conservation:

$$\nabla \cdot \vec{v} = 0 \tag{2}$$

$$\rho \frac{\partial \vec{v}}{\partial t} + \rho \vec{v} \cdot \nabla \vec{v} = -\nabla p + \mu \nabla^2 \vec{v} \tag{3}$$

Blood is assumed as homogeneous Newtonian fluid, having constant density and dynamic viscosity respectively equal to 1060 $kg \cdot m^{-3}$ and 0.0033 $kg \cdot m^{-1} \cdot s^{-1}$.

Equations (2) and (3) are solved under the following boundary conditions: no-slip on vessel wall and stent surface, prescribed velocity at the inlet and pressure at the outlet. The simulations are performed using the commercial code STAR-CCM+ 8.02.011, which solves the fluid-dynamics equations through the finite volume method. The SIMPLE algorithm is employed to solve the pressure-velocity coupling and the simulations are carried on until the convergence is reached. A second order implicit time-stepping method is used for the unsteady simulations, which are done for two cardiac cycles (2 sec), with a fixed time step of 5 ms, which guaranties a Courant number smaller than 0.5 for all the time steps. Only the second cycle results are recorded, while the first cycle is used to initialize the solution.

3.1 Steady simulation

In steady state, the mean velocity of 0.25 $m \cdot s^{-1}$, as measured in [31], is assumed on the inlet. Since the Reynolds number associated to this configuration is about 640, the flow regime is laminar and a Poiseuille velocity profile is prescribed at the inlet.

3.2 Transient simulation

In order to model the pulsatile blood flow, the theory of Womersley-Evans [32] is used to obtain the velocity profile, as shown in Fig. 4 a,

$$u(t,r) = 2u_0\left(1-\left(\frac{r}{R}\right)^2\right) + 2\sum_{m=1}^{N}\mathrm{Re}\left(U_m\Psi(\tau_m,r)e^{j\omega_m t}\right) \quad (4)$$

where

$$\Psi(\tau_m,r) = \frac{J_0(\tau_m) - J_0(\tau_m r/R)}{J_0(\tau_m) - J_1(\tau_m)/\tau_m} \quad (5)$$

and

$$\tau_m = j^{\frac{3}{2}}R\sqrt{\frac{\rho}{\mu}\omega_m} = j^{\frac{3}{2}}\alpha_m \quad (6)$$

J_0 and J_1 are the zeroth and first order Bessel functions of first kind, α_m are the Womersley numbers of order m, $\mathrm{Re}(\ )$ is the real part of a complex number, $j=\sqrt{-1}$ and U_m the Fourier coefficients of the pulsatile mean velocity profile, from the Eco Doppler measurements of [31]. By using the Fast Fourier Transform algorithm (FFT), the mean value and the first six harmonics are extracted and used to reconstruct the velocity profile. The same procedure is applied to reconstruct the pressure waveform on the outlet, presented in Fig. 4 b.

4. Hemodynamic variables

The most significant fluid dynamics factor which affects vessel remodeling is the wall shear stress (WSS). Other parameters, which, according to the literature [2, 7, 27, 32-33], are related to intimal hyperplasia (IH) and are useful in locating critical hemodynamic points, are studied as well.

The time-averaged wall shear stress (TAWSS) can be used to measure the cumulative effects

of WSS within a cardiac cycles and is defined as:

$$TAWSS = \frac{1}{T_o}\int_{T_o} \tau_w dt \tag{7}$$

The oscillatory shear index (OSI), defined as

$$OSI = \frac{1}{2}\left(1 - \left|\int_{T_o} \tau_w dt\right| \Big/ \int_{T_o} |\tau_w| dt\right) \tag{8}$$

is employed to measure the deviation of WSS from its average during the cycle.

The relative residence time (RRT), introduced in [7], identifies the regions of the wall subject to a stagnant flow and is defined as:

$$RTT = \left(\frac{1}{T_o}\int_{T_o} |\tau_w| dt\right)^{-1} \tag{9}$$

The wall is more prone to infiltrate cells and macromolecules where is higher the relative residence time, RRT, measured in Pa^{-1}, but it gives a relative measure of the time spent by the fluid in the vicinity of the wall. Hence, the absolute values of RRT are not important themselves, but give an indication of the regions prone to infiltration.

5. Results

5.1 **Steady simulations and mesh validation**

The results of the WSS, averaged over the vessel section, are shown in Fig. 5-8 for the two stents. The solution has been validated against three different grids. Figures 5 and 6 presents the results for a vessel without residual stenosis while Fig. 7 and 8 for a vessel with residual stenosis.

More than 200 slices are extracted by intersecting the vessel wall with parallel axial planes and the resulting data are interpolated by splines. In order to show the mesh independence of WSS,

according to [27], the steady simulations are performed for each stent with three different meshes (named mesh-1, mesh-2 and mesh-3) of respectively $5 \cdot 10^5$, 10^6, $2 \cdot 10^6$, cells. Since the last two meshes offer comparable results, the intermediate mesh has been used for the unsteady state simulations.

Figures 5 and 6 show a repeating pattern for the WSS, with peaks and valleys corresponding, respectively, to planes intersecting mostly the intra-strut area (where WSS is greater) and to planes intersecting regions of low WSS, located on the struts. Indeed, for a Newtonian fluid, the WSS only depends on the symmetric part of the velocity gradient at the wall, which strongly diminishes in proximity of the struts. This is due to the deceleration of the fluid impinging on an obstacle leaning on a wall. When the blood flow meets the edge of the strut, the streamlines, originally adhering to the wall, detach from it at a certain distance. A recirculation region is formed between the strut's wall and the detachment point, whose amplitude depends on the Reynolds number: the smaller it is, the wider is the recirculation region. The stent causes a geometrical discontinuity in the endothelium wall and a consequent loss of charge. The presence of these recirculation regions increases the residence time of macrophages and macromolecules on the endothelium and increase the probability of uptaking by intimal smooth muscle cells.

The results concerning the averaged WSS in presence of a 30% stenosis are shown in Fig. 7 and 8 as well. The reduction of the diameter provokes a pressure drop and a consequent acceleration of the fluid. Since the WSS is, in first approximation, inversely proportional to the section diameter and directly proportional to the fluid speed, the WSS increases in the chocked section. Downstream this region, the diameter increases and so the WSS diminishes. If the slope of the wall, downstream the chocking section, is high enough, a streamline detachment is present and a consequent recirculation region, which contributes to lower the WSS besides the geometrical changes.

Figure 7 shows that at a distance of approximately 8 mm from the center of the stent the

WSS starts to increase, as compared to the case without stenosis. It should be noted that the maximum WSS, which has a peak value of 2.66 Pa, does not correspond to the top of the stenosis but is 2.3 mm before, because both the axial and transversal velocities change more rapidly before the maximum height of the stenosis. After this point, the WSS decreases with some local peaks and valleys due to the struts, which disappear 1.5 mm after the vessel center. The WSS reaches a minimum value of 0.081 Pa at 5.1 mm from the vessel center and after that, gradually increases. A similar behavior can be observed in Fig. 8 for the stent S2. The WSS starts to increase at 9 mm before the center of the vessel, then it reaches the maximum value of 2.8 Pa at 1.9 mm before the vessel center, and then it decreases to the minimum monotonically, except a small plateau around the center of the vessel. The minimum of 0.11 Pa is reached at 6.5 mm as well. It must be remarked that the WSS in the stent S2 has a smoother profile compared to S1.

The similarity in the behavior of the two stents suggests that in the presence of a stenosis, the degree of stenosis plays a more important role in the fluid dynamics, compared to the stent geometry. The stenosis has a significant effect in terms of WSS reduction, causing an abrupt drop below the critical value of 0.5 Pa. This takes place downstream and is due to the presence of a stagnation region after the stenosis. The narrowing has the effect of amplifying the WSS in the central region, without exceeding 7 Pa, which is the value above which thrombogenic effects may take place [35-36].

In both fully expanded stents the mean WSS value is kept in the physiological range of 0.5 - 7 Pa, which is usually found in medium and large arteries [34-36]. Nevertheless from the computational data, the stent S2, peak-to-peak, seems to have a better behavior compared to the stent S1, peak-to-valley, since the WSS pattern is smoother, its average value is higher and the variance lower, indicating that this design alters less the fluid flow.

5.2 Unsteady state.

Unsteady state simulations, performed on an entire cardiac cycle, show large variations in terms of WSS minimum and maximum values. However, except the systolic peak, the WSS pattern does not exhibit great differences, and thus time averaged physiological parameters (OSI, RRT) are presented to take into account the cumulative effects of the fluid dynamics over the endothelium.

WSS maps of the endothelium reveal the presence of stagnation regions around the struts, where the WSS is low. In Fig. 9 the spatial distribution of WSS magnitude in the four configurations have been reported at three time steps: 0.0 s, 0.25 s and 0.53 s.

At the systolic peak, the pattern changes as well, showing that the region downstream the stenosis is always subject to a relatively low wall shear stress, while the WSS increases upstream. This is because the increase in flow rate broadens the extent of the recirculation region as well, in order that the WSS changes in direction but its modulus remains quite low.

In presence of the residual stenosis, the WSS in the choking region has the same pattern as the fully expanded stent and exhibit a high peak, corresponding to the minimum section and a much lower value downstream the narrowing. The WSS starts to grow again only when the flow attaches to the wall. The most significant role on the haemo-dynamics disturbance seems to be still played by the narrowing, while the different stent design influences the WSS patterns only at a minor extent.

OSI index is used to measure the oscillation of WSS from its mean direction. The OSI assumes value equal to 0 where the WSS has always the same direction during the cycle and 0.5 when the WSS mean value is 0 Pa. The simulations in the two straight vessels are shown in Fig. 10 and reveal a low value of OSI only near the struts, while in the intra-strut area this value is close to 0. It has been shown in [35, 37], that there is a correlation between atherosclerosis pathogenesis and OSI only for values between 0.1 and 0.5, thus in this case OSI is far from the critical range. Higher values of OSI can be observed in the small curvature formed by strut tips and connectors, where the

fluid is trapped as in Fig. 10 a.

In the configuration peak-to-peak, the peaks are arranged opposite one another, and this makes the stent mesh made from a hexagonal pattern. Between the vertices of the mesh there is a distance such that a region in which the motion is relatively undisturbed occurs.

The configuration peak-to-valley is more rugged than the peak-to-peak one. The stent mesh has “arrowhead” design, which provides an approximately constant distance between the opposite edges. Nevertheless, if this distance is not too long, and the velocity is big enough, the mesh can act as a roughness and favors the presence of recirculating regions and so inverted flow. This is in disagreement with Berry et al. [22], who suggested that a finer mesh could disturb the flow more than a coarser one. From our results it appears that, in physiological conditions, i.e. Re=640 according to [31], the stent S1 produces more recirculating regions compared to S2.

The OSI becomes more relevant when a stenosis exists, as shown by Fig. 12, with high values between 0.2 and 0.5. Our results show that a 30% reduction of the cross-section area is sufficient to provoke a boundary layer detachment after the stenosis. A wide recirculation region is present downstream the stenosis. There are no major differences in the OSI pattern of the two stents when a 30% stenosis is over-imposed, although even in this case the stent S2 appears to have slightly small OSI values compared to S1.

The relative time spent by the fluid in proximity of a certain region is measured by the RRT. This index estimates the probability of macromolecules to penetrate in the sub-endothelial space. OSI and RRT are mathematically related by the following equation:

$$RRT = \left(\left(1 - 2OSI \right) TAWSS \right)^{-1} \tag{10}$$

which means that the RRT has greater values in regions where OSI is closer to 0.5, and where the time averaged WSS is low. Thus the RRT is useful in locating low and oscillating regions for the

WSS, while the OSI gives information about the WSS oscillation. The same information can be extracted from RRT maps: high values appear in the same location of the OSI, between the strut tips and in the distal vessel. The RRT also carries information about time averaged WSS, and can be useful in locating both oscillating and low shear stresses, that seem to represent regions prone to atherosclerosis.

Figures 13 and 14 show the RRT of the two stents. Figure 13 presents the RRT of the two stents in the vessel without stenosis, showing that the RTT increases where is present the stent and decreases on the vessel wall, because the RTT is proportional to the reciprocal of the time averaged wall shear stress, and this variable is considerably lower in the region where the stent is inserted. Moreover, since the WSS pattern is wavy in the stented region, RRT shows some peaks. The RRT presents higher values for the peak-to-valley configuration than the peak-to-peak one. This is due to the low TAWSS present in the region covered by the stent S1 and by higher values of OSI that are uniform in the case S2.

In Fig. 14 the RRT in the stenosed vessel is shown. This variable show evident differences in the performances of the two stents configurations. The RRT for the stent S1 is much higher than that for the S2 one. Both lowering of TAWSS and increasing of OSI, due to the stagnation region, contribute to its increase. The previous results about the WSS and the OSI suggested already that the configuration peak-to-peak had a better fluid-dynamic behavior, compared to the peak-to-valley, but the results were not as evident as in the RRT case.

6. Discussion

The present work investigates the fluid dynamics in two different stent configurations, peak-to-valley (S1) and peak-to-peak (S2), in a fully expanded situation and when a 30% restenosis is present. Numerical simulations are carried out in order to evaluate the fluid dynamics conditions which can promote atherosclerotic events, when a self-expanding bare metal stents (SE-BMS) is

applied.

The performances of the two devices are analyzed in steady state by means of WSS and unsteady state, through WSS, OSI and RRT. The analysis in the straight vessels shows that the performances of the peak-to-peak configuration gives better results compared to the peak-to-valley one. In the configuration peak-to-valley, S1, the WSS is lower and OSI and RRT are higher compared to the peak-to-peak, S2 one.

The analysis of the two configurations in a stenosed vessel, as far as WSS and OSI is concerned, show that the two stents have approximately the same behavior. However the RRT is much bigger in the peak-to valley configuration, which, in agreement with the results in the straight vessel, suggest that the S2 configuration is performing better even in the presence of stenosis.

Gori and Boghi [27-29] suggested that the struts with connectors parallel to the mean flow can reduce the restenosis rate, which could be in contrast with the previous result, pointing out a better behavior for S2. Indeed, although none of the stents investigated in this study has connectors, the peak-to-valley design has the struts more aligned to the flow direction and should result in a lower flow disturbance. Nonetheless, the higher spatial density of the struts in the S1 configuration could have the most significant effect, hiding the effect produced by the strut alignment with the mean flow.

It can be pointed out that in the choice of the best device, the mechanical properties, such as the flexibility, must be taken into account as well. In particular, the configuration S1, peak-to-peak, is more rigid and does not fit too well the vessel boundary. This is coherent with the result shown in [27-29], where the more rigid configuration can give better fluid dynamics behavior.

The results obtained in the stenosed configuration, showed that even a small residual restenosis, which is completely asymptomatic in terms of blood delivery to the head, could expose the endothelium to hazardous WSS distributions. The choice of 30% as percent of residual stenosis

is arbitrary, but is not a big value compared to the cases studied in [10].

The numerical approach of the present work has some limitations, especially for what concerns the domain. The simulations are performed by assuming the artery as a straight rigid vessel, while diseased carotid arteries have non-zero compliance and a more complex geometry. The rigid vessel assumptions should not affect the results because in animals, stent implants limit wall compliance to zero [27-29]. Yet, the complexity of the real geometry affects more the fluid dynamics, as documented in the literature [1-6], where the relationship between stenosis and particular geometric loci, like bifurcations, has been documented. Nevertheless, the study of a simplified geometry allows understanding the influence of each parameter on the WSS and gives a glimpse of what can take place in a more complex one. Moreover, if we can show that, for a given restenosis, critical hemodynamic conditions occur on a simplified geometry, we can easily guess that the situation will be even worst in a skewed geometry, thus this limitation should not affect the results validity.

7. Conclusion

From the present numerical simulations, it can be concluded that the application of self-stent expandable has a twofold effect: on one hand it can reduce the graft failure rate, limiting artery injury caused by balloon inflation (at high pressures of about 12-16 bar), and, on the other hand, the residual narrowing could represent a critical region for the hemodynamics. This stenosis, even if not harmful for the patient, could disrupt the blood flow downstream the narrowing, exposing the endothelium to hazardous WSS, which could result in the long-term in neo-intimal proliferation, promoting the restenosis of the artery.

Long-term medical follow-up, for this fairly new implant, and in vivo experiments could help to point out whether the negative effects over fluid dynamics, due to residual stenosis, are more significant than the benefic effects produced by the less traumatic implant technique. Moreover, the

simulation is a powerful tool to evaluate which is the best hemodynamic configuration. In this work and in [27-29] it looks like the better hemodynamic configuration is the less compliant one. This contradiction may be overcome in a more realistic configuration where the struts are deformed in a non-symmetric way. A study on a realistic geometry may give completely different results in terms of mechanical and hemodynamic properties.

The effort in the stent design should be by conjugating good mechanical and hemodynamic properties. Further studies are required to investigate other configurations and a more realistic arterial geometry.

Acknowledgements

We thank Dr Leon Williams of Cranfield University for the support given with SolidWorks. The contribution of Mr. F. Iori in the numerical tests is gratefully acknowledged.

References

1. R. Russell, Atherosclerosis — An Inflammatory Disease, *New England Journal of Medicine*, vol. 340, no. 2, pp. 115–126, 1999.

2. C. G. Caro, J. M. Fitz-Gerald and R. C. Schroter, Arterial wall shear and distribution of early atheroma in man, *Nature*, vol. 223, pp. 1159-60, 1969.

3. C. G. Caro, J. M. Fitz-Gerald and R. C. Schroter, Atheroma: a new hypothesis, *Br. Med. J.*, vol. *2*, pp. 651, 1971.

4. C. G. Caro, J. M. Fitz-Gerald and R. C. Schroter, Atheroma and arterial wall shear. Observation, correlation and proposal of a shear dependent mass transfer mechanism for atherogenesis, *Proc. R. Soc. London B. Biol. Sci.*, vol. *177*, pp. 109-159, 1971.

5. P. F. Davies, Flow-mediated endothelial mechanotransduction, *Physiol. Rev.*, vol. *75*, no. 3, pp. 519-60, 1995.

6. M. A. J. Gimbrone and G. Garca-Cardena, Vascular endothelium, hemodynamics, and the pathobiology of atherosclerosis. *Cardiovasc. Pathol.*, vol. 22, no. 1, pp. 9-15, 2013.

7. H. A. Himburg, D. M. Grzybowski, A. L. Hazel, J. A. Lamack, X. Li and M. H. Friedman, Spatial comparison between wall shear stress measures and porcine arterial endothelial permeability, *A. J. Physiol Heart Circ Physiol*, vol. *286*, pp. 1916-1922, 2004.

8. S. Park, D. Lee, W. Chung, D. H. Lee and D. C. Suh, Long-term Outcomes of Drug-eluting Stents in Symptomatic Intracranial Stenosis, *Neurointervention*, vol. 8, no. 1, pp. 9-14, 2013.

9. B. P. Mwipatayi, S. Thomas, D. Angel, J. Wong and V. Vijayan, Stent outcomes for infrapopliteal arterial occlusive disease, *Vascular.*, vol. 21, no. 3, pp. 121-128, 2013.

10. S. P. Lownie, D. M. Pelz, D. H. Lee, S. Men, I. Gulka and P. Kalapos, Efficacy of treatment of severe carotid bifurcation stenosis by using self-expanding stents without deliberate use of angioplasty balloons. *AJNR Am J Neuroradiol*, vol. 26, 1241-1248, 2005.

11. M. Schillinger, M. Exner, W. Mlekusch, M. Haumer, R. Ahmadi, H. Rumpold, O. Wagner and E. Minar, Inflammatory response to stent implantation: differences in femoropopliteal, iliac, and carotid arteries, *Vascular and Interventional Radiology*, vol. 224, no. 2, pp. 529-35, 2002.

12. A. Farb, D. K. Weber, F. D. Kolodgie, A. P. Burke and R. Virmani, Morphological predictors of restenosis after coronary stenting in humans, *Circulation*, vol. 105, pp. 2974-2980, 2002.

13. T. S. Riles, A. Lieberman, I. Kopelman and A. M. Imparato, Symptoms, stenosis, and bruit: interrelationships in carotid artery disease, Arch Surg, vol. 116, no. 2, pp. 218-220, 1981.

14. F. Gori and A. Boghi, Image-Based Computational Fluid Dynamics in a Carotid Artery, *ASME International Mechanical Engineering Congress and Exposition, Proceedings*, vol. 2, pp. 123-128, 2009.

15. F. Gori and A. Boghi, On a New Turbulent Energy Equation with Variable Thermal Conductivity, *ASME International Mechanical Engineering Congress and Exposition, Proceedings,* vol. 2, pp. 813-818, 2008.

16. F. Gori, A. Boghi, Two new differential equations of turbulent dissipation rate and apparent viscosity for non-Newtonian fluids, *International Communications in Heat and Mass Transfer*, vol. 38, pp. 696-703, 2011.

17. F. Gori, A. Boghi, A Three Dimensional Exact Equation For The Turbulent Dissipation Rate of Generalized Newtonian Fluids, *International Communications in Heat and Mass Transfer,* vol. 39, pp. 477-485, 2012.

18. F. Gori and A. Boghi, On a New Passive Scalar Equation with Variable Thermal Diffusivity, *ASME International Mechanical Engineering Congress and Exposition, Proceedings,* vol. 2, pp. 495-500, 2008.

19. F. Gori, A. Boghi, On a New Passive Scalar Equation with Variable Mass Diffusivity: Flow Between Parallel Plates, *Journal of Fluid Engineering, Transactions of the ASME*, v. 132, n. 11, art. No. 111202, Nov. 2010

20. G. S. Roubin, The status of carotid stenting, *AJNR Am J Neuroradiol,* vol. 20, pp. 1378-1381, 1999.

21. P. Bergeron, T. De Chaumaray, J. Gay and V. Douillez, Endovascular treatment of thoracic aortic aneurysms, *J Cardiovasc Surg,* vol. 44, no. 3, pp. 349-361, 2003.

22. J. L. Berry, A. Santamarina, J. E. Moore Jr, S.R. Routh and W. D. Routh, Experimental and Computational Flow Evaluation of Coronary Stents, *Annals of Biomedical Eng.*, vol. 28, no. 4, 386-398, 2000.

23. L. Lanoye, M. De Beule, C. Dewijngaert, P. Segers, P. Van Impe and P. Verdonck, The Influence of the Strut Section Shape on the Flow Field in a Newly Stented Right Coronary Artery, *The 56th National Congress of Theoretical and Applied Mechanics, NCTAM*, 2006.

24. T. Seo, L. G. Schachter and A. I. Barakat, Computational Study of Fluid Mechanical Disturbance Induced by Endovascular Stents, *Annals of Biomedical Eng.*, vol. 33, no. 4, pp. 444-456, 2005.

25. F. LaDisa, L. E. Olson, I. Guler, D. A. Hettrick, S. H. Audi, J. R. Kersten , D. C. Warltier , P. S. Pagel, Stent Design Properties and Deployment Ratio Influence Indexes of Wall Shear Stress: A Three-Dimensional Computational Fluid Dynamics Investigation within a Normal Artery. *J. Appl. Physiology*, vol. 97, pp. 424-430, 2004.

26. J. F. LaDisa, D. A. Hettrick, L. E. Olson, I. Guler, E. R. Gross, T. T. Kress, J. R. Kersten, D. C. Warltier, P. S. Pagel, Coronary Stent Implantation Alters Coronary Artery Hemodynamics and Wall Shear Stress during Maximal Vasodilation, *J. Appl. Physiology*, vol. 93, pp. 1393-1946, 2002.

27. F. Gori, A. Boghi, Three-Dimensional Numerical Simulation of Blood Flow in Two Coronary Stents, *Numerical Heat Transfer*, vol. 59, no. 4, pp. 231-246, 2011.

28. F. Gori, A. Boghi, M. Amitrano, Three-Dimensional Numerical Simulation of the Fluid Dynamics in a Coronary Stent, *ASME International Mechanical Engineering Congress and Exposition Proceedings,* vol. 2, pp. 407-411, 2009.

29. F. Gori, A. Boghi, Three-Dimensional Numerical Simulation of non-Newtonian Blood in two Coronary Stents, *14th International Heat Transfer Conference, IHTC14,* vol. 1, pp. 109-114, 2010.

30. S. Muller-Hullsbeck, P. J. Schafer, N. Charalambous, S. R. Schaffner, M. Heller, T. Jahnke, Comparison of Carotid Stents: An In-Vitro Experiment Focusing on Stent Desig, *J. Endovasc. Ther.*, vol. 16, no. 2, pp. 168-177, 2009.

31. P. Buratti, Analysis of Doppler blood flow velocity in carotid arteries for the detection of atherosclerotic plaques. Master Thesis, Politecnico di Milano, 2011.

32. J. R. Womersley, Method for the calculation of velocity, rate of flow and viscous drag in arteries when pressure gradient is known, *J. Appl. Physiol*., vol. 127, pp. 553-563, 1955.

33. G. Coppola and C. Caro, Arterial geometry, flow pattern, wall shear and mass transport: potential physiological significance, *J R Soc Interface*, vol. 6, pp. 519-528, 2009.

34. A. Farb, D. K. Weber, F. D. Kolodgie, A. P. Burke, R. Virmani, Morphological Predictors of Restenosis after Coronary Stenting in Humans, *Circulation*, vol. 105, pp. 2974-2980, 2002.

35 D. N. Ku, D. P. Giddens, C. K. Zarins and S. Glagov, Pulsatile Flow, and Atherosclerosis in the Human Carotid Bifurcation, Positive Correlation between Plaque Location and Low Oscillating Shear Stress, *Arteriosclerosis,* vol. 5, pp. 293–302, 1985.

36. A. M. Malek, S. L. Alper and S. Izumo, Hemodynamic Shear Stress and its Role in Atherosclerosis, *JAMA*, vol. 282, no. 21, pp. 2035–2042, 1999.

37. X. He and D. N. Ku, Pulsatile flow in the human left coronary artery bifurcation: average conditions, *Journal of Biomechanical Engineering,* vol. 118, no. 1, pp. 74–82, 1996.

NOMENCLATURE

Dimensional

p dynamic pressure, Pa.

r radial coordinate, m.

R inlet radious, m.

R_2 minimum radius, m.

R_1 maximum radius, m.

RTT the relative residence time, 1/Pa.

t current time, s.

T_o observation time, s.

TAWSS time averaged wall shear stress, Pa.

$u(t,r)$ inlet velocity, m/s.

u_0 average inlet velocity, m/s.

U_m Fourier coefficients of the pulsatile mean velocity profile, m/s.

$\vec{v}$ velocity field, m/s.

Non-Dimensional

j imaginary unit.

J_0 zeroth order Bessel function of first kind.

J_1 first order Bessel functions of first kind.

OSI oscillatory shear index.

$P(\%)$ percentage of restenosis.

$\mathrm{Re}(\ )$ is the real part of a complex number.

Greek

α_m Womersley numbers of order m.

ρ density, kg/m3.

μ dynamic viscosity, Pa*s.

$\Psi(\tau_m, r)$ scaled Bessel function.

ω_m dimensional pulsation of order m.

τ_m non-dimensional pulsation of order m.

τ_w wall shear stress N/m2

Captions to figures.

Figure 1: Stent configurations: a) Peak-to-valley (S1). b) Peak-to-peak (S2).

Figure 2: Geometry of stenosed vessel reconstructed by polynomial approximation.

Figure 3: Detail of mesh.

Figure 4: a) velocity profile. b) pressure profile.

Figure 5: WSS spatial distribution in S1 stent without residual stenosis for the three meshes.

Figure 6: WSS spatial distribution in S2 stent without residual stenosis for the three meshes.

Figure 7: WSS spatial distribution in S1 stent with residual stenosis for the three meshes.

Figure 8: WSS spatial distribution in S2 stent with residual stenosis for the three meshes.

Figure 9: WSS spatial distribution for S1 and S2 in a non-stenosed vessel, at three different time instant.

Figure 10: WSS spatial distribution for S1 and S2 in a stenosed vessel, at three different time instant.

Figure 11: OSI distribution without residual stenosis for S1 (a) and S2 (b).

Figure 12: OSI distribution with residual stenosis for S1 (a) and S2 (b).

Figure 13: RRT distribution without residual stenosis.

Figure 14: OSI distribution with residual stenosis.

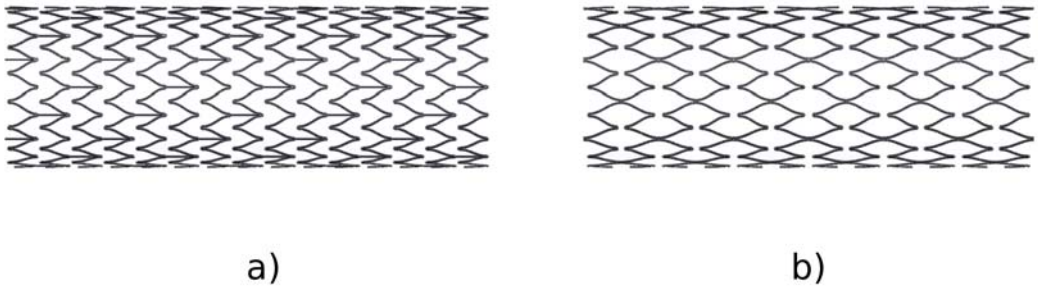

Figure 1: Stent configurations: a) Peak-to-valley (S1). b) Peak-to-peak (S2).

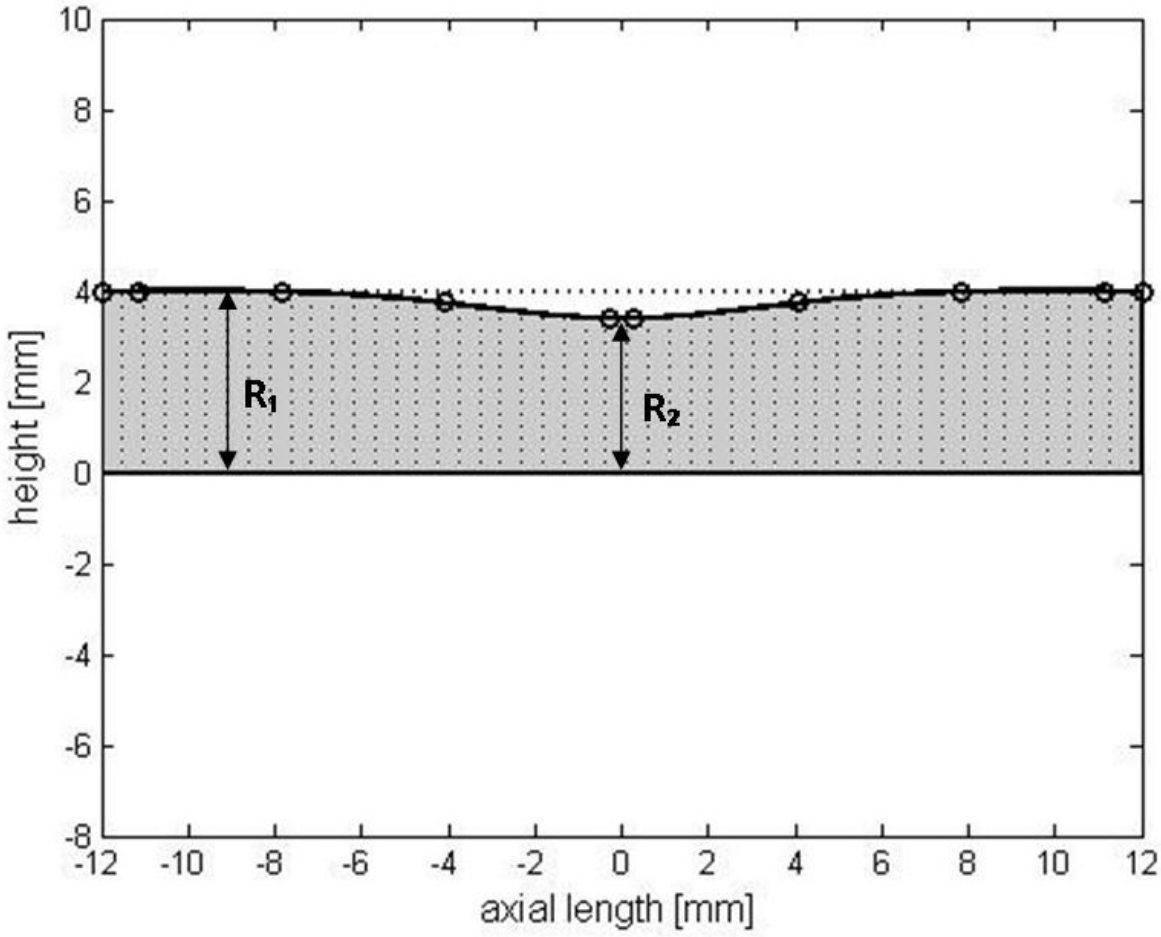

Figure 2: Geometry of stenosed vessel reconstructed by polynomial approximation.

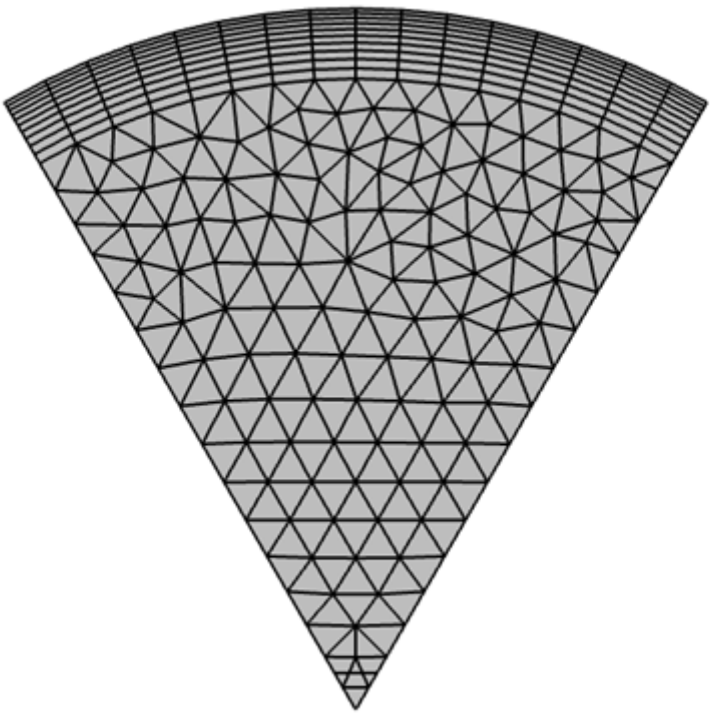

Figure 3: Detail of mesh.

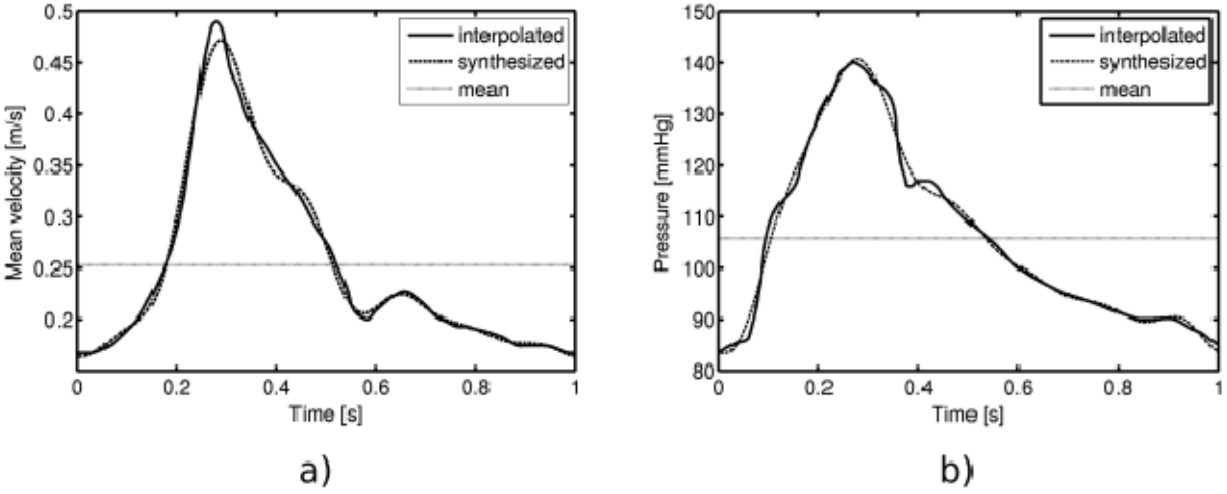

Figure 4: a) velocity profile. b) pressure profile.

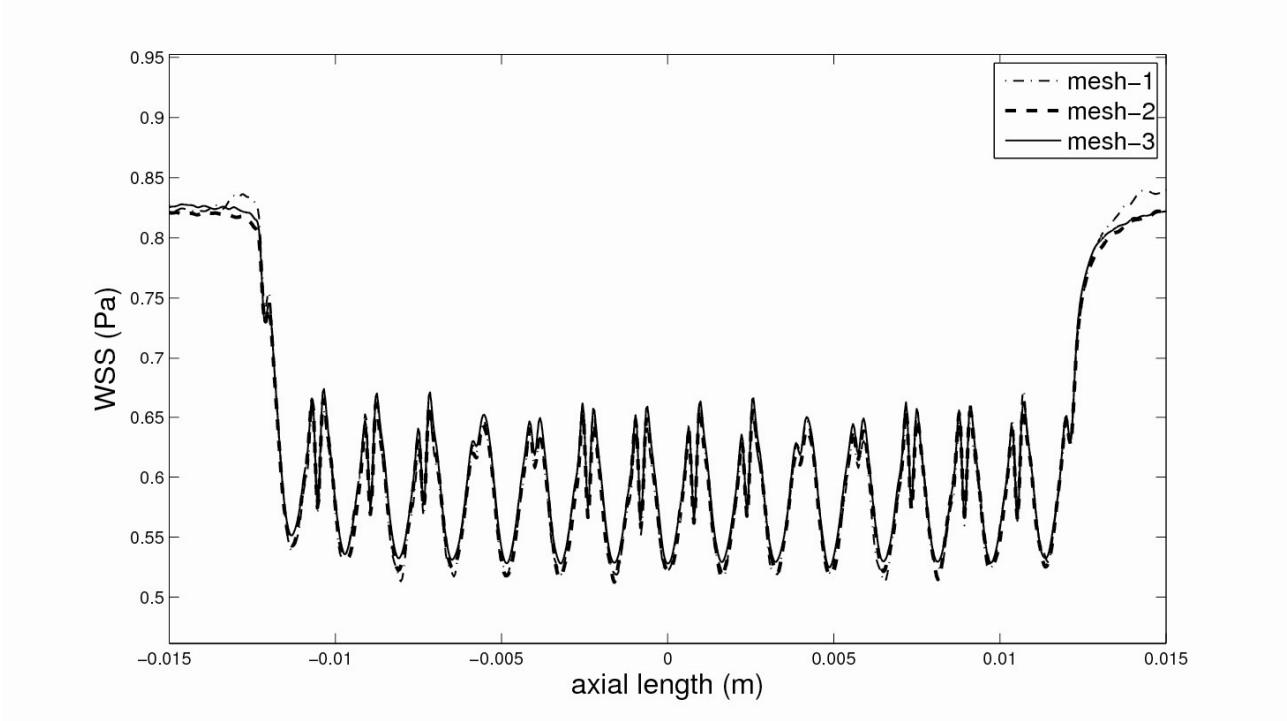

Figure 5: WSS spatial distribution in S1 stent without residual stenosis for the three meshes.

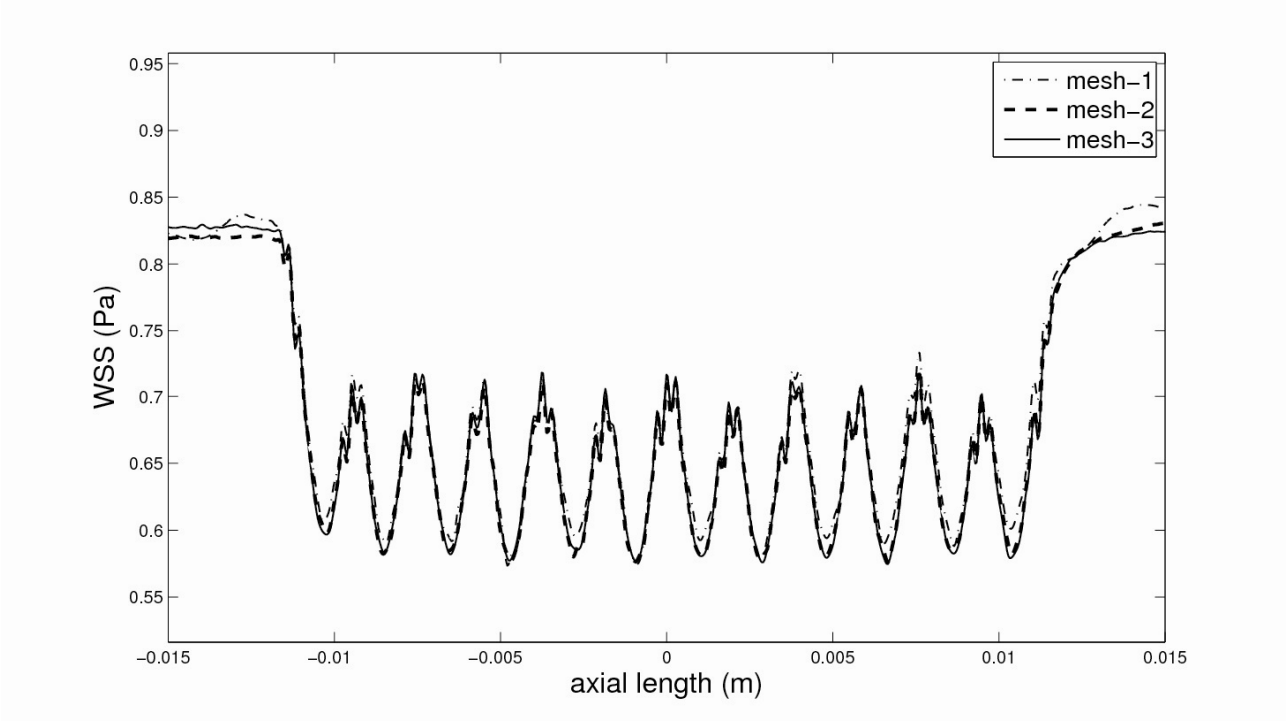

Figure 6: WSS spatial distribution in S2 stent without residual stenosis for the three meshes.

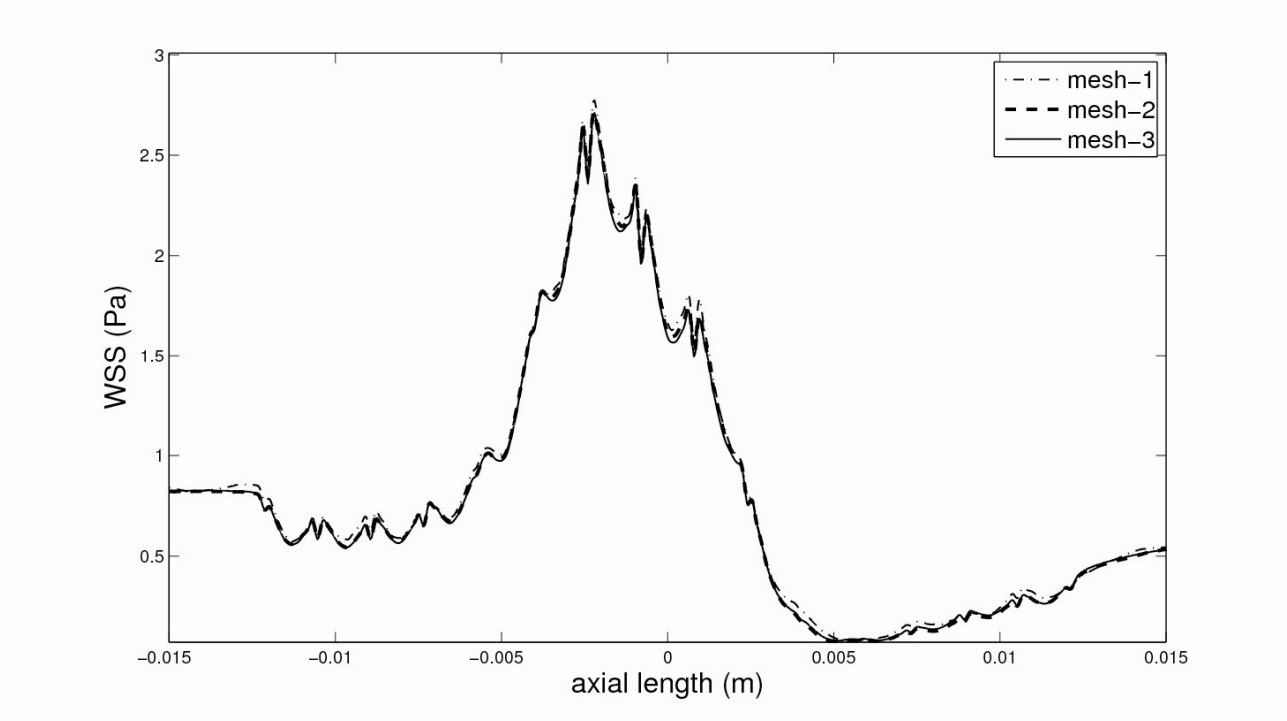

Figure 7: WSS spatial distribution in S1 stent with residual stenosis for the three meshes.

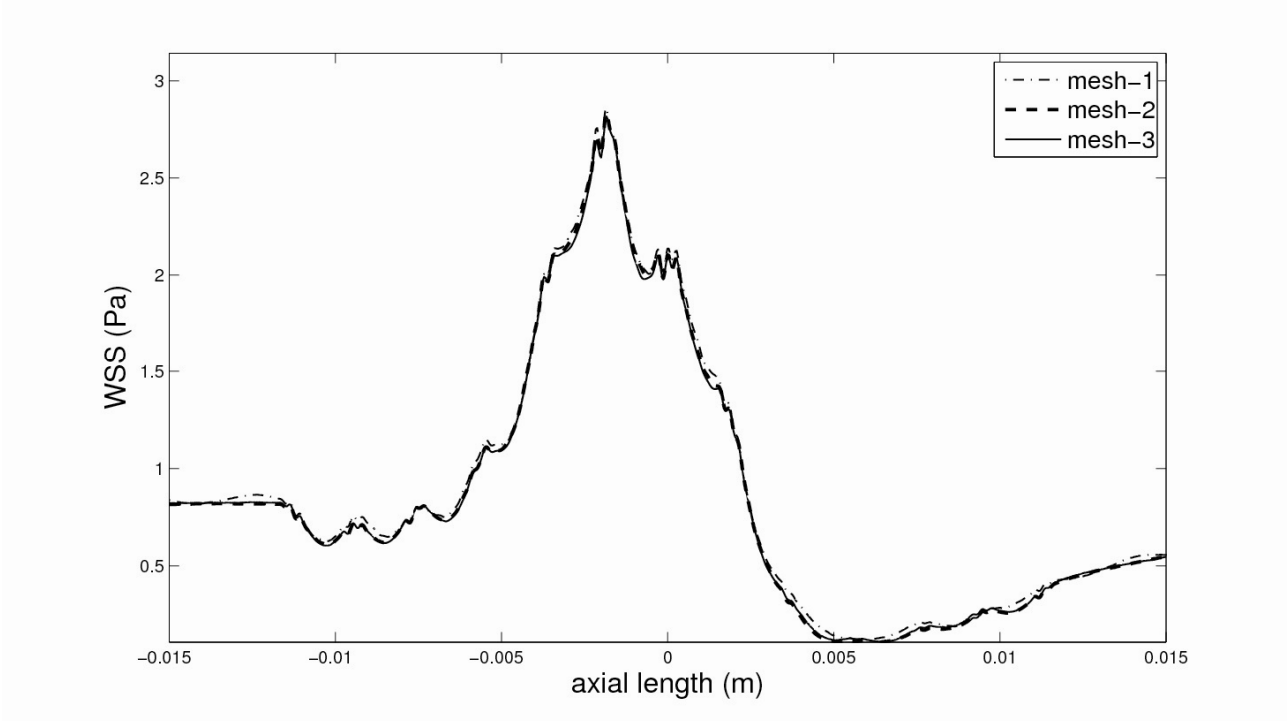

Figure 8: WSS spatial distribution in S2 stent with residual stenosis for the three meshes.

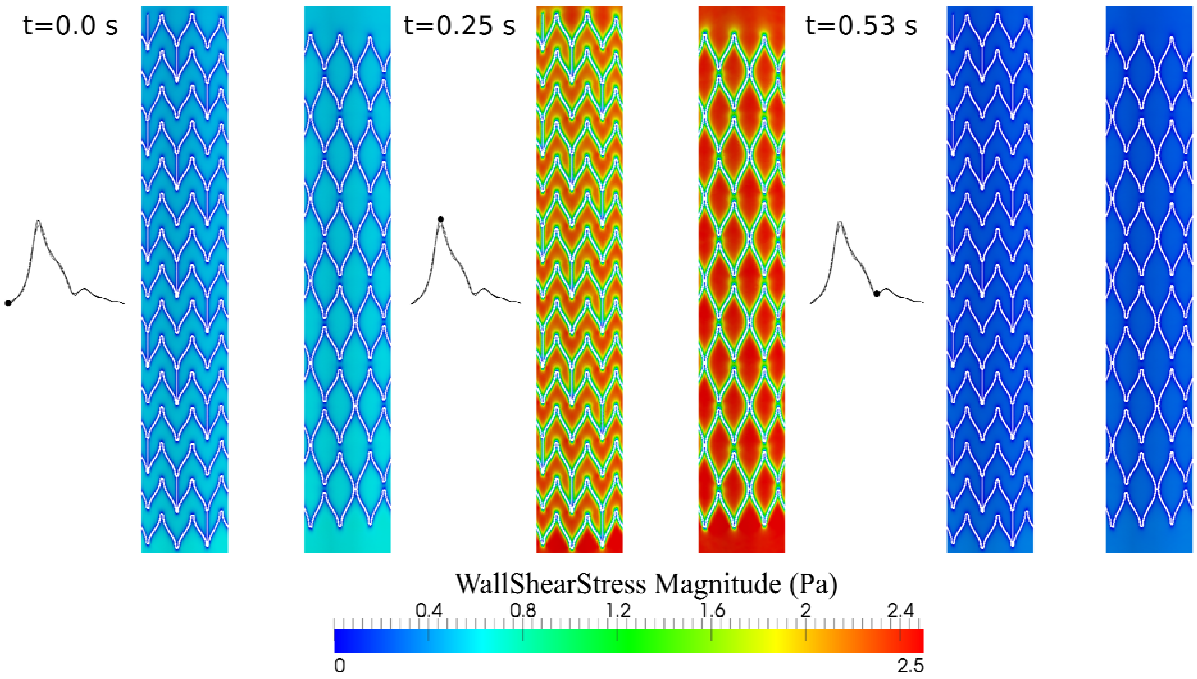

Figure 9: WSS spatial distribution for S1 and S2 in a non-stenosed vessel, at three different time instant.

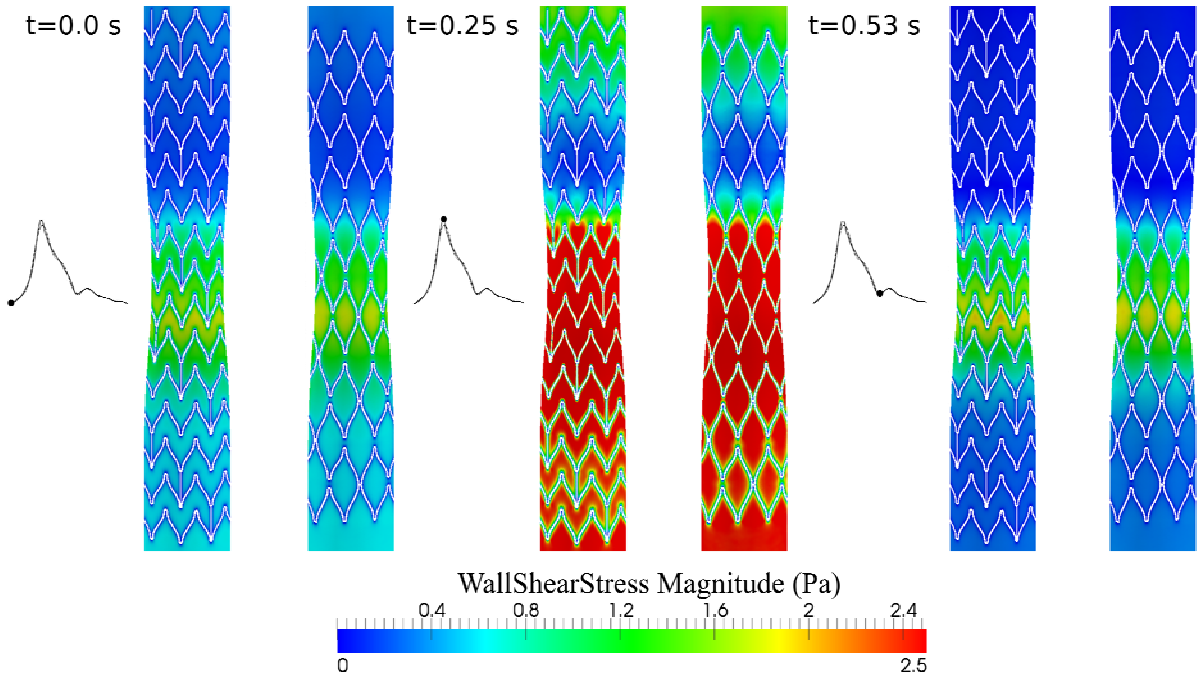

Figure 10: WSS spatial distribution for S1 and S2 in a stenosed vessel, at three different time instant.

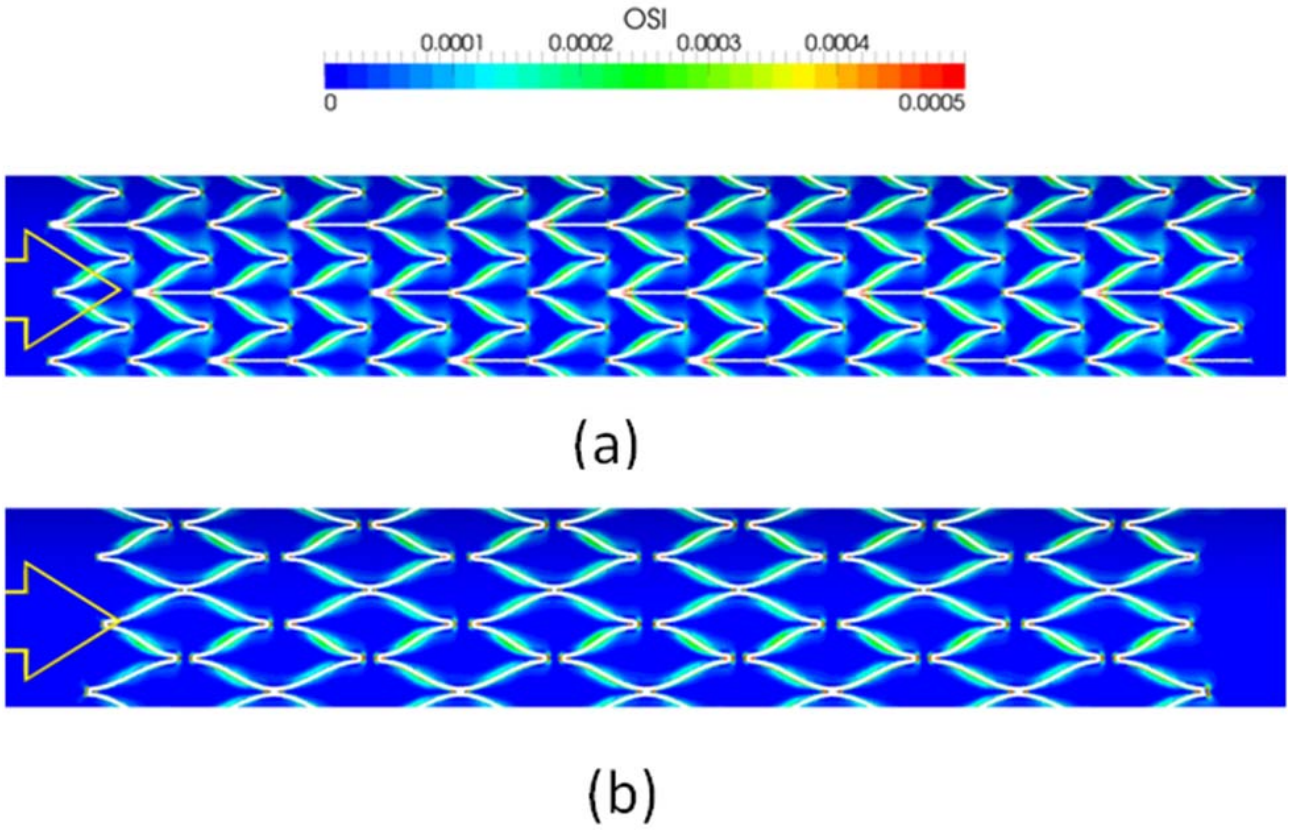

Figure 11: OSI distribution without residual stenosis for S1 (a) and S2 (b).

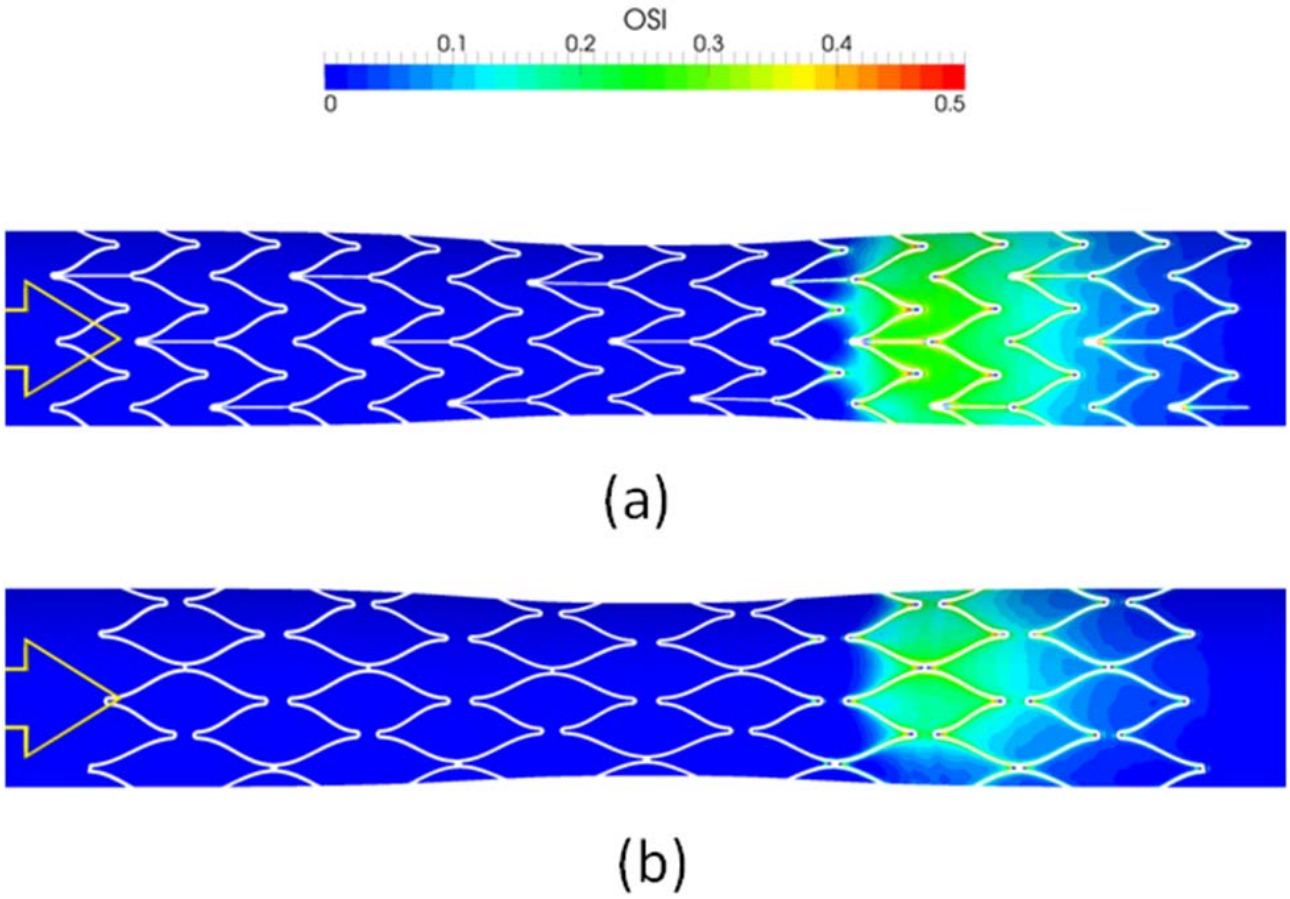

Figure 12: OSI distribution with residual stenosis for S1 (a) and S2 (b).

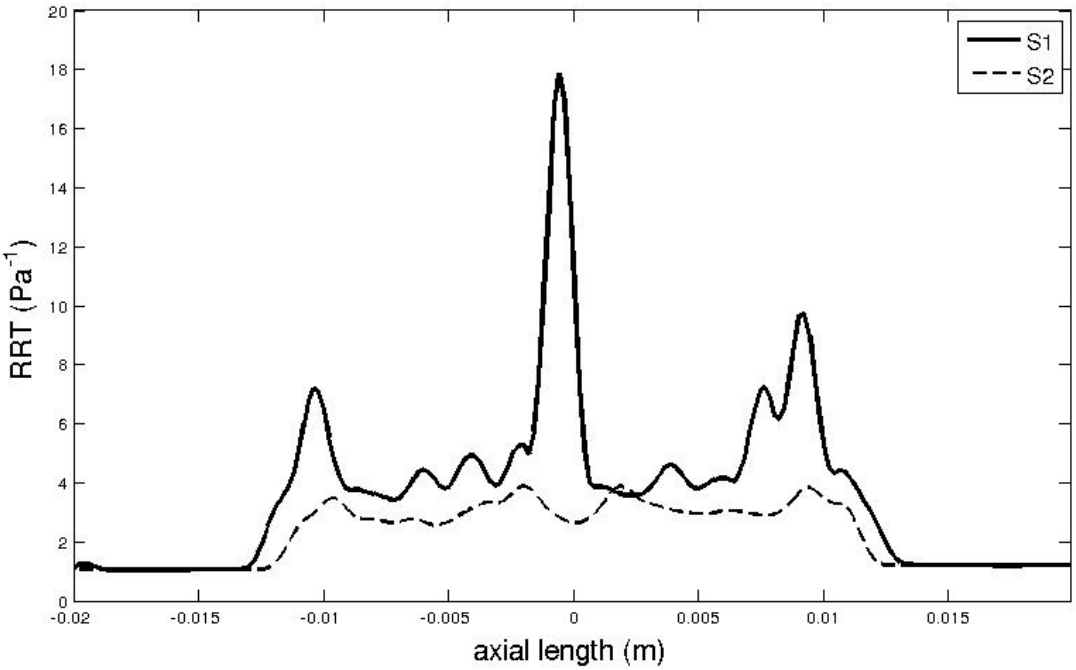

Figure 13: RRT distribution without residual stenosis.

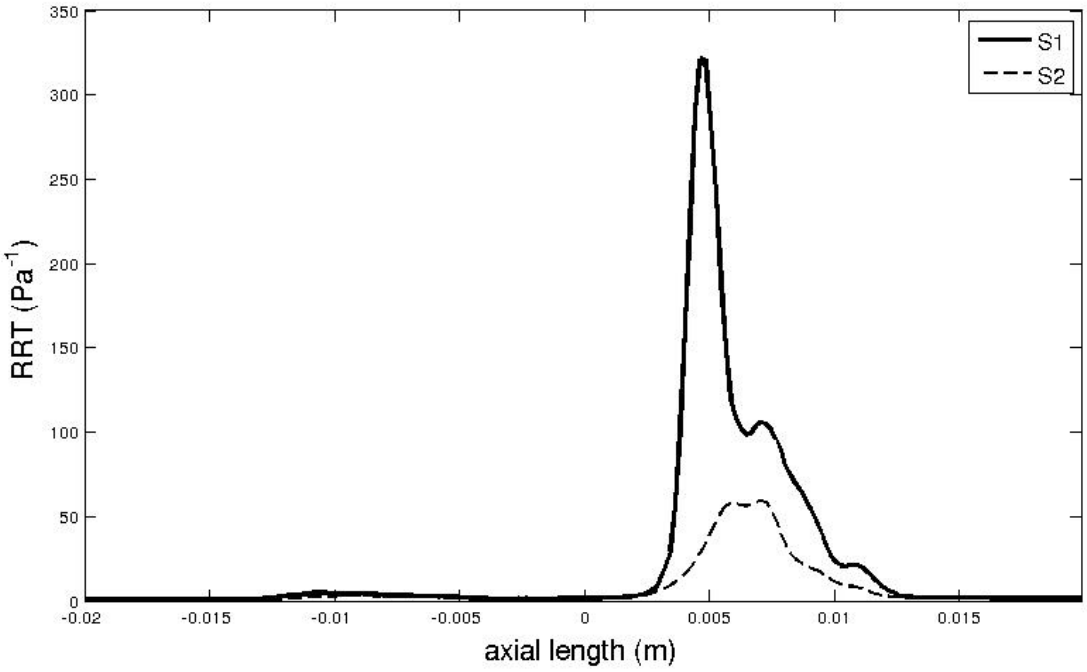

Figure 14: OSI distribution with residual stenosis.